文章编号：1001-9014(2023)06-0883-12

DOI：10. 11972/j. issn. 1001-9014. 2023. 06. 022

A 0.3 W@4.2 K high-capacity lightweight cryogenic system for space BIB detection

CHU Jin-Jian[1,2], LIU Shao-Shuai[1,2*], WANG Peng[1,2], DING Lei[1], XIAO Yun-Long[1,2], YIN Wang[1,2], CHEN Zhi-Chao[1], SHA Xin-Quan[1], JIANG Zhen-Hua[1,2], WU Yi-Nong[1,2*]

(1. Shanghai Institute of Technical Physics, Chinese Academy of Sciences, Shanghai 200083, China;
2. University of Chinese Academy of Sciences, Beijing 100049, China)

Abstract: Large-array BIB detectors have been the subject of extensive research due to their high quantum efficiency and low dark current, particularly for space applications such as the JWST, which was launched in 2021 and has made numerous significant astronomical observations. A stable, efficient, and lightweight temperature zone liquid helium cryogenic system is essential to the operation of the BIB detectors. The helium JT cryocooler is a trend that aims to meet the cooling requirements of a liquid helium temperature zone in space while supplanting the traditional, large-volume liquid helium dewar. To simultaneously increase the cooling capacity at 4. 2 K and reduce its weight, a high-capacity, lightweight 4. 2 K cryocooler with a cooling power of 0. 3 W@4. 2 K is proposed. Experiments on the previous 0. 1 W at 4. 1 K prototype of the cryogenic system have validated the system´s design method. Different cooling methods are used in different cooling temperature zones to achieve the efficiency and lightness of cooling. A new integrated Stirling cryocooler was developed to provide efficient pre-cooling at 80 K, with a cooling capacity of 15 W and a weight of only 4. 5 kg. A 0. 9 W at 15 K active piston phase-shifting pulse tube cryocooler is used to improve the efficiency of the second-stage pre-cooling. The developing cryogenic system can provide a cooling capacity of 0. 3 W at 4. 2 K with a power consumption of less than 1. 8 kW by coupling the helium JT cycle. It will provide the essential guarantee for the large-scale BIB detection required for infrared astronomical observation, which is undergoing rapid development.

Key words: cryogenic system, space BIB detection, stirling, pulse tube, JT, liquid helium, multi-stage cryocooler

用于空间BIB探测器的0.3 W@4.2 K大冷量轻量化低温系统

褚晋简[1,2], 刘少帅[1,2*], 王 鹏[1,2], 丁 磊[1], 肖云龙[1,2], 殷 旺[1,2], 陈志超[1], 沙鑫权[1], 蒋珍华[1,2], 吴亦农[1,2*]

(1. 中国科学院上海技术物理研究所,上海 200083;
2. 中国科学院大学,北京 100049)

摘要:大阵列BIB探测器由于其高量子效率和低暗电流而成为广泛的研究对象,特别是在空间应用方向。如2021年发射的詹姆斯韦伯太空望远镜,它已经进行了许多重要的天文观测。一个稳定、高效、轻量化的液氦温区低温系统对BIB探测器的运行至关重要。氦节流制冷机可取代传统的大容积液氦杜瓦,能满足空间液氦温区的制冷要求。为了同时提高4.2 K的制冷量并减轻重量,提出了一种0.3 W@4.2 K的大冷量轻量化的4.2 K低温制冷系统。并且在现有0.1 W@4.1 K制冷量的低温系统上进行实验,验证了该系统的设计方法。在不同的冷却温度区采用不同的冷却方法,以实现冷却的高效性和轻便性。开发了一个新的集成斯特林制冷机,在80 K时提供高效的一级预冷,制冷量为15 W,重量仅为4.5 kg;二级预冷采用主动活塞调相的15 K脉管制

Received date: 2023- 03- 08, **revised date**: 2023- 06- 07 **收稿日期**:2023- 03- 08,**修回日期**:2023- 06- 07

Foundation items: Supported by the Hundred Talents Program of the Chinese Academy of Sciences, the National Natural Science Foundation Projects (51806231), the Strategic Priority Research Program of Chinese Academy of Sciences (XDB35000000, XDB35040102)

Biography: CHU Jin-Jian (1999-), female, Altay Xinjiang Province, Ph. D. Candidate. Research area involves liquid helium temperature zone JT refrigeration technology. E-mail: chujinjian@mail. sitp. ac. cn

* **Corresponding author**: E-mail: liushaoshuai@mail. sitp. ac. cn

冷机,制冷量为0.9 W。此多级低温制冷系统通过耦合氦气JT循环,可以在4.2 K时提供0.3 W的制冷量,输入功低于1.8 kW。此系统将为正在快速发展的红外天文观测所需的空间BIB探测器提供保障。

关 键 词:低温系统;空间BIB探测器;斯特林;脉冲管;焦汤节流;液氦;多级制冷机

中图分类号:TN215 **文献标识码**: A

Introduction

Using the transition of impurity levels in semiconductor materials, Blocked Impurity Band (BIB) detectors can cover the 5-30 μm band, with the cut-off wavelength of Si:Ga up to 20 microns [1] and Si:As (or Si:P) up to 28 and 35 microns, respectively. The advantages of the large surface array BIB detector include a low dark current, a broad response spectrum, a high quantum efficiency, and excellent radiation resistance. The large surface array BIB detector satisfies the application requirements of infrared astronomy and a few specialized observation requirements in an exceptional fashion. The temperature zone of liquid helium (4.2 K) is required for the high-efficiency operation of the BIB detector, which would suffer from unacceptable thermal noise due to the impurity ionization at higher temperatures [2-6].

The cryocooler at 4.2 K that is commonly used on the ground is the GM cryocooler, which has a large weight and an oil compressor that is unsuitable for space use. Both the multi-stage Stirling pulse tube cryocooler (SPTC) and the helium Joule-Thomson cryocooler (JTC) can achieve the BIB detector′s required cooling capacity of 4.2 K [7-8]. Due to the advantages of no moving parts in the cold head and high reliability, the cryocooler has been an important direction of liquid helium temperature zone cryogenic technology used by the BIB large area array detector [9].

As can be seen in Table 1, in 1981, a two-stage Stirling cryocooler (SC) precooled JTC developed by the Spectroscopy Laboratory of the Lebedev Institute of the Soviet Academy of Sciences (LPI/RAS) was successfully utilized in the 1977-launched Sayut-6 Space Station to provide 0.5 W@4.4 K for the infrared detectors in the BET-IM telescope [10]. The total weight is 127 kg, and the input power is 1.5 kW. Due to the compressor′s limitations, its service life cannot exceed 3000 hours. JAXA-SHI, Sumitomo Heavy Industries, obtained a 4 K JTC engineering prototype with two-stage SC pre-cooling at 4.57 K with 23 mW@4.57 K [11] in 2001. The maximum temperature fluctuation is 3 mK and the total weight is 40 kilograms. In 2006, NGST achieved 65 mW@6 K [12] with a three-stage SPTC precooled JTC designed for the ACTDP project. A three-stage SC precooled JTC designed by BALL is also capable of achieving 75 mW@6.2 K for ACTDP. The JWST project ultimately chose the three-stage SC precooled JTC designed by NGAS for MIRI [13-17]. The total power input is 473 W. Cooling time is 38 hours. JAXA has developed a 4K-class JTC with the required cooling power of 40 mW at 4.5 K and 10 mW at 1.7 K [18], respectively, for future next-generation space missions named ATHENA-X.

Besides, the stability of the operating temperature of the BIB detector has decisive significance for its high-performance infrared astronomical detection. This could be further attributed to the lower dark current and larger photoresponse at stable low temperatures. Due to the doping-induced bandgap narrowing effect and little impurity ionization energy, the sharp rise in dark current would be caused by even a tiny increase in temperature[19]. Temperature stability control of cryogenic systems is quite important for BIB detectors.

1 Design goals

In accordance with the long-term stability, low vibration, and deep cryogenic requirements of the large area array BIB detector, the first-stage Stirling cryocooler and the second-stage power recovery piston phase-modulated Stirling pulse tube cryocooler coupled with a helium JT technology system are proposed. A 300 mW@4.2 K JT cryocooler, which input power is @1.8 kW, is developed as a detector cryogenic component for the barrier impurity band (BIB). In comparison to the Soviet Union′s 0.5 W@4.2 K cryocooler (complete machine 127 kg), the JT system, in conjunction with piston phase-modulation technology and high-frequency ultra-long stroke compressor technology, significantly reduces overall machine weight and achieves high cooling capacity in a lightweight cryocooler (weight 30 kg). This technical path has advantages in the development of a cryo-

Table 1 Performance of 4.2 K cryocooler systems
表 1 4.2K低温制冷系统性能

Year	Institution	Cooling power	Input power	Detector	Cryocooler systems
1981	LPI/RAS	500 mW@4.4 K	1.5 kW	BET-IM	Two-stage SC+JT
2001	JAXA-SHI	23 mW@4.57 K	166 W	-	Two-stage SC+JT
2006	NGST-ACTDP	7.75 mW@4.5 K	229 W	-	Three-stage SPTC+JT
2007	BALL-ACTDP	75 mW@6.2 K	300 W	-	Three-stage SC+JT
2011	NGAS-ACTDP	113 mW@6.2 K	104 W	JWST-MIRI	Three-stage SPTC+JT
2014	TIPC/CAS	11.6 mW@4.5 K	473 W	-	Three-stage SPTC+JT
2021	JAXA	40 mW@4.5 K	90 W	ATHENA-X	Two-stage SC+JT

cooler with a large cooling capacity of 4.2 K, and its comprehensive indicators achieve international leadership status.

For this design, the cooling capacity should be a minimum of 0.3 W@4.2 K, the input power should not exceed 1.8 kW, and the weight better be less than 30 kg. When the cryocooler is designed with redundancy, the required input power is 1.6 kW. Due to the physical property deviation in the liquid helium temperature zone and the years of development experience of the unit, the cryogenic capacity is designed with more than 40% redundancy during thermal design, resulting in a cryogenic performance of 0.5 W at 4.2 K, as shown in Table 2.

Table 2　Design specification
表 2　设计参数

Parameters	Target values	Design values
Cooling capacity	≥0.3 W@4.2 K	0.5 W@4.2 K
Power consumption	≤1.8 kW	1.6 kW
Weight	≤30 kg	27 kg
Temperature Fluctuation	≤±2 mK(30 min)	≤±2 mK(60 min)

The design is depicted in Fig. 1, the first-stage cryocooler employs the existing XP-GXN SC, and the second stage cryocooler employs the existing two-stage SPTC optimization parameter structure. The main compressor and the cold finger are thermally coupled. The valve linear compressor (VLC) employs a symmetrical piston compression arrangement and optimizes the design for weight reduction. Reduce the VLC's radial flutter force output. A helium-JT three-stage inter-wall regenerative heat exchanger uses a two-phase regenerative heat exchanger in microgravity to improve the heat exchange efficiency of the cryocooler, reduce the pressure drop loss at the low-pressure side, enhance the efficiency of the cryocooler, and achieve the miniaturization of a large cooling capacity [20].

2　Design considerations of the 0.3 W@4.2 K lightweight cryocooler system

2.1　Pre-cryocooler

To achieve 0.3 W@4.2 K, a new JT cryocooler (JTC) pre-cooling system has been compared and selected. Combining the advantages of a two-stage precooler and JT technology, designing JTC uses the thermal coupling method to realize efficient coupling between the precooler and JT system, combining the advantages of the precooler and JT technology at different temperature ranges, which is one of the best ways for the space 4.2 K large cooling capacity application.

Under the performance target of 0.3 W@4.2 K, the temperature of the second-stage Stirling-type pulse tube cryocooler (SPTC) is 15 K and the high-pressure is 1.6 MPa. The required mass flow can be calculated by the temperature of second-stage of SPTC and high-pressure. Since the high-pressure has the best value, When the pre-cooling temperature of the second-stage pulse tube is determined, the mass flow will decrease first and then increase for the given second-stage SPTC temperature, with a minimum value. Combined with the minimum power consumption relationship, the mass flow of the helium JTC is 45 mg/s. According to the design requirements and the optimal parameter matching relationship,

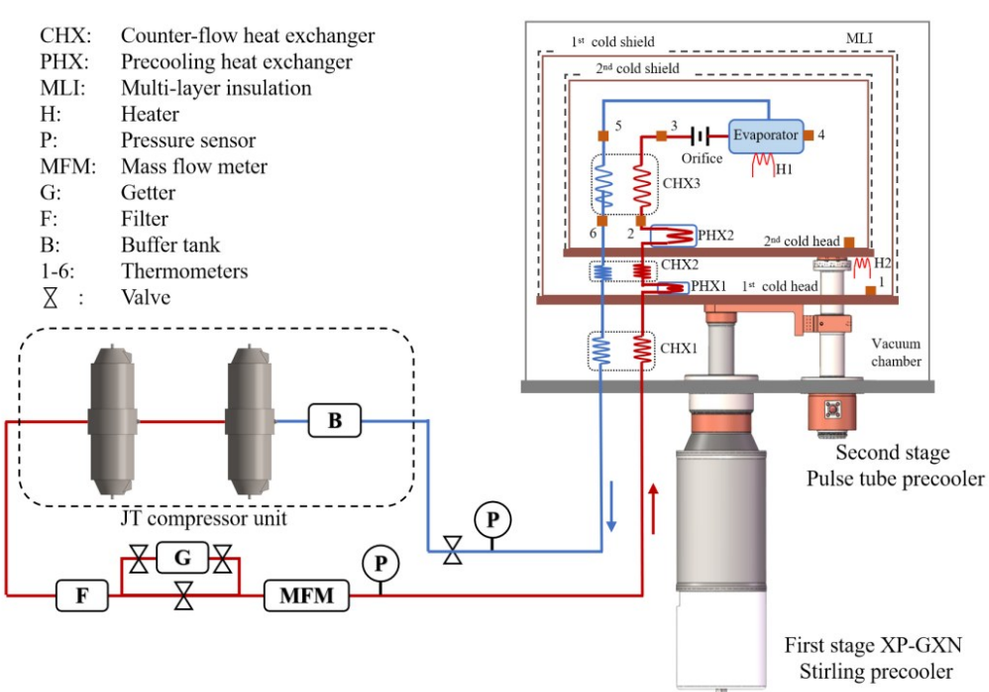

Fig. 1　4.2 K JT cryocooler system
图 1　4.2 K节流制冷系统图

it can be concluded that the pre-cooling capacity of the two-stage precooler should not be less than 4 W@80 K and 0.8 W@15 K. Considering redundancy and radiation heat loss, the required cooling capacity of two-stage precooler is determined as 15 W@80 K and 0.9 W@15 K.

The structure of the two-stage precooler used in this system is shown in Fig. 2. The first-stage is SC with the operating temperature of 80 K. The second-stage of the cryocooler is SPTC with the operating temperature of 15 K. The second-stage SPTC adopts the coaxial structure to improve the compactness of the system and the phase shifter uses the active warm displacer with work-recovery (AWDW). The use of AWDW can improve the phase modulation ability in the liquid hydrogen temperature zone. In addition, the size of the phase shifter can be optimized to reduce the weight of the system.

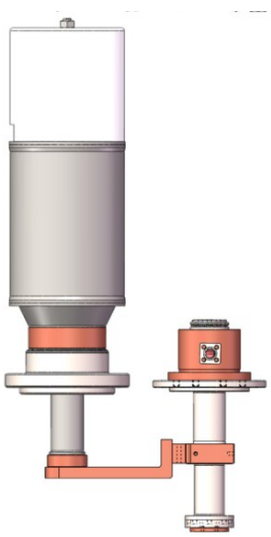

Fig. 2 Structure of the two-stage precooler
图2 两级预冷结构图

The use of AWDW in the second-stage could achieve lower temperature, higher performance and higher efficiency [21]. AWDW can actively adjust the phase relationship in the cold finger while recovering the acoustic power at the hot end of the SPTC. The force analysis of the piston of AWDW is carried out. The piston is subjected to gas force, spring force and damping force, as well as a motor driving force. The gas force is divided into the dynamic pressure from the expansion chamber and the dynamic pressure from the work-recovery chamber. Under the combined action of these forces, the piston moves in an inertial sine. The vector motion equation of the piston movement is shown in equation (1) [22-23].

$$m_d\ddot{\tilde{x}}_d = \tilde{F} - \frac{\pi}{4}D_d^2\tilde{P} - f_d\dot{\tilde{x}}_d - k_d\tilde{x}_d\,, \tag{1}$$

$$= \tilde{F} - \frac{\pi}{4}D_d^2\widetilde{P}_e + \frac{\pi}{4}\left(D_d^2 - D_{rod}^2\right)\widetilde{P}_r - f_d\dot{\tilde{x}}_d - k_d\tilde{x}_d$$

$\widetilde{P}_e$ represents the dynamic pressure from the expansion chamber, and $\widetilde{P}_r$ represents the dynamic pressure from the work-recovery chamber. The gas force is also divided into gas stiffness and gas damping, which are composed of the expansion cavity and recovery cavity:

$$F_{kgas} = k_{gas}\tilde{x} = \left(\left|\widetilde{P}_e\right|\frac{\pi D_d^2}{4\widetilde{x}_d}\cos\theta_e\right)\tilde{x} - \left(\left|\widetilde{P}_r\right|\frac{\pi\left(D_d^2 - D_{rod}^2\right)}{4\widetilde{x}_d}\cos\theta_r\right)\tilde{x}\,, \tag{2}$$

$$F_{fgas} = f_{gas}\dot{\tilde{x}} = \left(\left|\widetilde{P}_e\right|\frac{\pi D_d^2}{4(2\pi f)\widetilde{x}_d}\sin\theta_e\right)\dot{\tilde{x}} + \left(\left|\widetilde{P}_r\right|\frac{\pi\left(D_d^2 - D_{rod}^2\right)}{4(2\pi f)\widetilde{x}_d}\sin\theta_r\right)\dot{\tilde{x}}\,. \tag{3}$$

Because the gas stiffness is larger than the damping value, the gas force stiffness from the work-recovery chamber is opposite to the gas force stiffness from the expansion chamber. The gas stiffness in the expansion chamber can be significantly reduced by reasonable design [24]. At this time, the gas force can be changed by adjusting the impedance of the hot end of the cold finger. Besides, the diameter of the push rod which drives the piston movement will become an important design structural parameter. It can be seen from equation (2) and equation (3) that the area of the gas force from the work recovery chamber can be changed by adjusting the rod diameter, which can optimize the resultant force of the gas force. The resultant force of the gas force is reduced, and the motor force required for the piston to maintain inertial sine motion can also be reduced to a minimum. The structure size of the motor can be reduced to achieve lightweight [25].

Since the acoustic work at the hot end of the SPTC in the temperature range of 15 K is small. A thermally coupled two-stage SPTC has been developed which uses an active warm displacer (AWD) without work-recovery as a phase shifter, as shown in Fig. 3. Experiments were carried out using a single-stage SPTC as the pre-cooling machine.

Fig. 3 Photo of 15 K second-stage pulse tube cryocooler
图3 第二级15 K脉管制冷机实物图

Through experimental tests, the second-stage SPTC can obtain the maximum cooling capacity at the second stage when the frequency is 30 Hz. Figure 4 shows the change of rCOP (relative Carnot efficiency) and cooling capacity with the phase difference between the piston of

AWD and the main compressor [26]. The efficiency and cooling capacity first increase and then decrease with the increase of phase difference. The maximum rCOP of the whole machine appears at 20 Hz, which can obtain 0.74 W cooling capacity, and the total input electric power is 294 W, as we can see in Fig. 4(a). In Fig. 4(b), the maximum cooling capacity of 15 K is 0.91 W, the total input electric power is 386 W, and the rCOP of the whole machine is 4.45%. At this time, the specific Carnot efficiency of the whole machine is 4.79% [27].

The single-stage SC is an integrated pneumatic structure with a free displacer. Its pneumatic displacer moves sinusoidally with the driving piston and maintains a certain phase difference with the compressor driving piston through structural design to achieve cooling capacity. The free displacer performs regular sinusoidal motion under the combined effects of the gas force, the spring force caused by the leaf spring, and the friction resistance. According to the stress analysis, the differential equation of motion vector can be written, as shown in equation (4) [28-29]:

$$m_e\ddot{\tilde{x}}_e = A_{e1}\tilde{P} - A_{e2}\tilde{P} - \left(A_{e1} - A_{e2}\right)P_m - f_e\dot{\tilde{x}}_e - k_e\tilde{x}_e \ , \quad (4)$$

$\tilde{P}$ is the instantaneous pressure, $\widetilde{P_m}$ is the pressure of the back cavity, and it is assumed that the pressure at the expansion chamber, regenerator, and the compression chamber is the same.

The theoretical cooling capacity of SC is equal to the expansion work. The expression is as follows (5):

$$Q_e = \frac{\omega}{2\pi}\oint\tilde{P}\cdot\frac{d\widetilde{V_{e1}}}{dt}dt = \frac{1}{2}|P||V_{e1}|cos\theta_e \ . \quad (5)$$

The theoretical cooling capacity can be expressed as:

$$Q_e = \frac{A_{e1}}{2}|P|^2\frac{\left(A_{e1} - A_{e2}\right)\omega^2 f_e}{\left(k_e - \omega^2 m_e\right)^2 + \left(\omega f_e\right)^2} \ . \quad (6)$$

In addition, f_e is the mechanical damping affected by the assembly process, and m_e is the mass of the actuator affected by the motor structure design. It can be seen from equation (6) that for pneumatic SC k_e mechanical stiffness k_e and difference of sectional area $\left(A_{e1} - A_{e2}\right)$ are the two key parameters that affect the cooling capacity of pneumatic SC. The former is mainly controlled by the leaf spring structure and pieces, while the latter is controlled by the displacer rod diameter.

A numerical simulation software is used to model and analyze. After the optimization of the regenerator structural parameters, the influence of the mechanical stiffness and the diameter of the push rod on the performance of the cryocooler is mainly considered.

Figure 5 shows the calculation results with different mechanical stiffness. The calculation results show that the increase in the leaf spring stiffness leads to an increase in cooling capacity and COP. When the stiffness increases to a certain value, the movement of driving piston is difficult to push the displacer to move, and the cooling capacity and overall efficiency begin to decrease gradually. In addition, due to the limitation of leaf spring assembly in the actual situations and lightweight design, the selected stiffness is 12000 *N/m*, the cooling capacity is 16 W, and COP is close to the optimal value.

With an increase in the diameter of the push rod, the area difference between the two ends of the displacer increases, leading to the change in the displacer pneumatic force. Therefore, the displacement and phase of the pneumatic displacer are mainly affected by the diameter of the push rod. Thus, there are optimal diameters of the push rod to obtain maximum cooling capacity and performance efficiency. The smaller diameter of the push rod, the smaller the mass of the mover, which is beneficial for reducing the weight of the displacer. The calculated suitable rod diameter within the optimal range is around 7 mm, as this time the COP is approximately 13%, as we can see in Fig. 6.

Within this cryogenic system, the vibration of the precooler is a crucial factor that requires our attention.

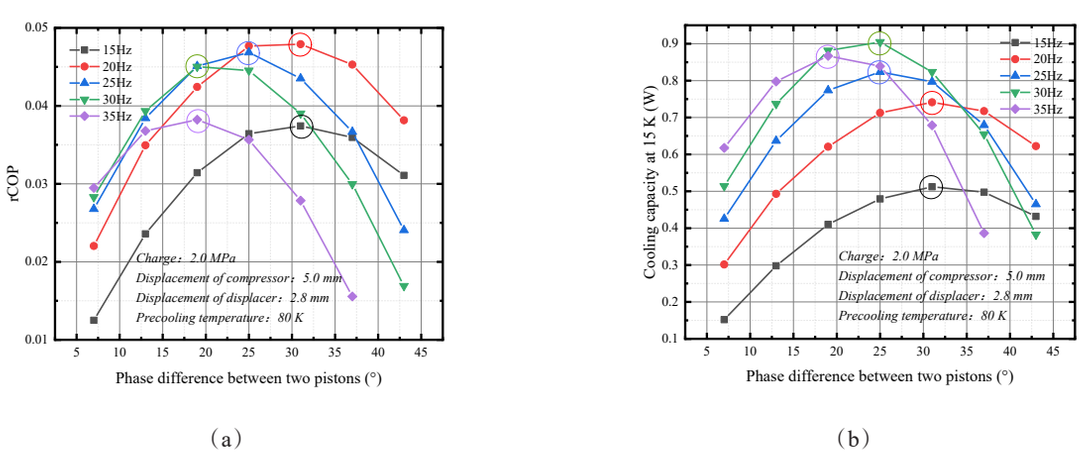

(a)　(b)

Fig. 4　(a)Effect of frequency on 15 K rCOP, (b)Effect of frequency on 15 K cooling capacity
图 4　(a) 15 K时频率对rCOP的影响, (b) 15 K时频率对制冷量的影响

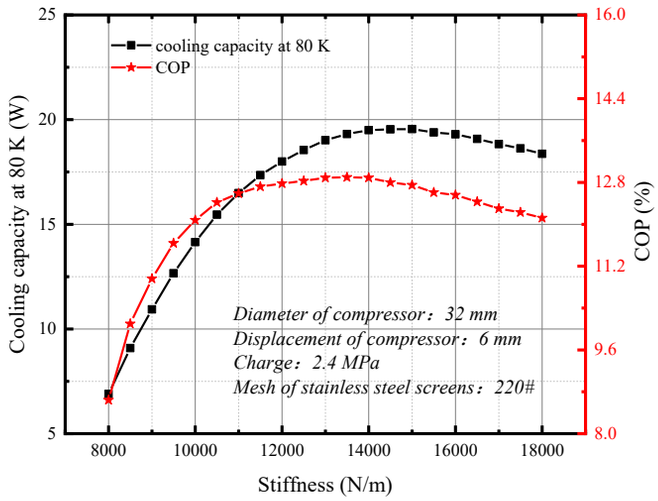

Fig. 5 Effect of mechanical stiffness on Stirling cryocooler
图 5 机械刚度对斯特林制冷机的影响

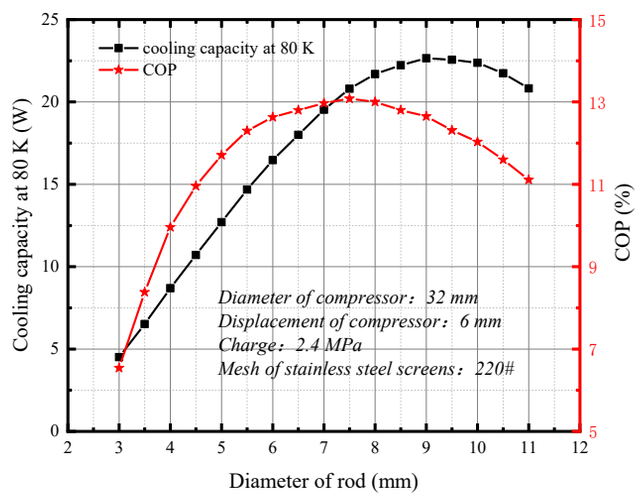

Fig. 6 Influence of the diameter of the push rod on Stirling cryocooler
图 6 推杆直径对斯特林制冷机的影响

This is due to low vibration is beneficial to the stable operation of the coupled BIB detector. Taking the first-stage Stirling cryocooler, which has relatively large vibrations, as an example, an active vibration damper has been adopted to reduce its vibration output and solve the problem. The basic principle of a vibration damper is the momentum balance method. Active vibration damping uses an electrically driven actuator to achieve momentum balance through active control. During operation, momentum balance is achieved by adjusting the driving phase and voltage amplitude between the damper and the compression piston. The technology has been successfully applied in multiple space projects by our research team. During the experiments, it was verified that the first-stage Stirling cryocooler's individual vibration output was less than 1N. Similar active vibration reduction technology can also be used for pulse tube compressors and valve linear compressors. Besides, by adding small vibration dampers to the system platform, low vibration output of the system can be ensured.

2.2 Valved linear compressor with high-pressure ratio and large mass flow rate

According to the decomposed indicators 0.5 W@4.2 K cryogenic performance: when the secondary precooling temperature is 15 K, the valved linear compressor (VLC) needs to provide the JTC with a pressure of 0.1 MPa at the evaporator. It is preliminarily estimated that there is a pressure drop of about 10~20 kPa without the casing pressure drop loss. Considering that in practical application, the design margin given for the index parameters is 18%. The design demand index of VLC is 0.08 MPa for low-pressure, 1.6 MPa for high-pressure, 18.9 for total pressure ratio, 53 mg/s for mass flow, 40 Hz for operation frequency, and 15% for volumetric efficiency.

According to the existing structure and experiment, a double-piston opposed compressor structure is adopted and the valve group is external, which obtains the cooling capacity of 110 mW at 4.2 K. According to the decomposition index, the power consumption of VLC does not exceed 0.8 kW and the weight does not exceed 10 kg. That is to meet the performance while achieving the compactness and lightweight of VLC units.

The gas load force of the linear compressor is the combined force of the working gas on the front and rear faces of the piston [30].

$$f_g(t) = A_p(P_c(t) - P_b)\,, \tag{7}$$

A_p is the cross-sectional area of the piston; P_b is the shell pressure; $P_c(t)$ is the time-varying gas pressure in the compressor chamber.

In the VLC, the gas force is the only factor that produces the higher harmonic component in the mechanical vibration system. The higher harmonics are attenuated and can be approximated by the first harmonic component. The gas load force changes periodically and can be expanded into the Fourier series. The simplified gas load force is:

$$F_g(t) = a_1\cos\omega t + b_1\sin\omega t + F_0\,, \tag{8}$$

$$a_1 = \frac{1}{\pi}\int_0^{2\pi} F_g(t)\cos(\omega t)d(\omega t)\,, \tag{9}$$

$$b_1 = \frac{1}{\pi}\int_0^{2\pi} F_g(t)\sin(\omega t)d(\omega t)\,, \tag{10}$$

$$F_0 = \frac{1}{\pi}\int_0^{2\pi} F_g(t)d(\omega t)\,. \tag{11}$$

The gas load force can be decomposed into 1 equivalent gas spring, 1 gas damping and 1 static force, and its expression is as follows:

$$F_g(t) = c_g\frac{dx}{dt} + k_g x + F_0\,, \tag{12}$$

$$k_g = -\frac{a_1}{X}\,, \tag{13}$$

$$c_g = \frac{b_1}{\omega X}\,. \tag{14}$$

The working process includes compression, exhaust, expansion, and suction.

During compression, the compressor chamber pressure increases and stops when it reaches θ_1. The piston continues to move and enters the exhaust phase. When $\theta_t = \pi$, the exhaust stops. During expansion, the compressor chamber pressure decreases and stops when it reaches θ_2. The piston continues to move and enters the suction phase. When $\theta_t = 2\pi$, the suction phase stops.

$$F_{g\text{-}P_1}(t) = (P_g(t) - P_{sc})A_P = \begin{cases} [(\dfrac{X_0 + X}{X_0 + x(t)})^n P_{cs} - P_0]A_P & 0 \leqslant \theta_t < \theta_1 \\ (P_{cd} - P_0)A_P & \theta_1 \leqslant \theta_t < \pi \\ [(\dfrac{X_0 - X}{X_0 + x(t)})^n P_{cd} - P_0]A_P & \pi \leqslant \theta_t < \theta_2 \\ (P_{cs} - P_0)A_P & \theta_2 \leqslant \theta_t < 2\pi \end{cases}, \tag{15}$$

where the VLC displacement is:

$$x(t) = X\cos(\theta)\,, \quad \theta = 2\pi\mathrm{ft} \tag{16}$$

where the phase angle of the compression phase θ_1 and the end phase angle of the expansion phase θ_2 are:

$$\begin{cases} \theta_1 = \arccos\left\{(\dfrac{1}{X})[(X_0 + X)(\dfrac{P_{cs}}{P_{cd}})^{\frac{1}{n}} - X_0]\right\} \\ \theta_2 = 2\pi - \arccos\left\{(\dfrac{1}{X})[(X_0 - X)(\dfrac{P_{cd}}{P_{cs}})^{\frac{1}{n}} - X_0]\right\} \end{cases}. \tag{17}$$

According to the thermal design, the first and second stage gas stiffness and its gas damping parameters are obtained. Combined with the mechanical damping and the leaf spring stiffness, the total stiffness and total damping are obtained. Maxwell is used to designing the motor and the miniaturization and optimization design of the motor can be carried out at the same time. By reducing the radial thickness of the inner pole, the outer diameter of the magnetic circuit is reduced, so that the motor current is close to the critical current value, which can minimize the motor volume and weight. By reducing the radial thickness of the inner pole, the trend of motor efficiency is obtained as follows in Fig. 7.

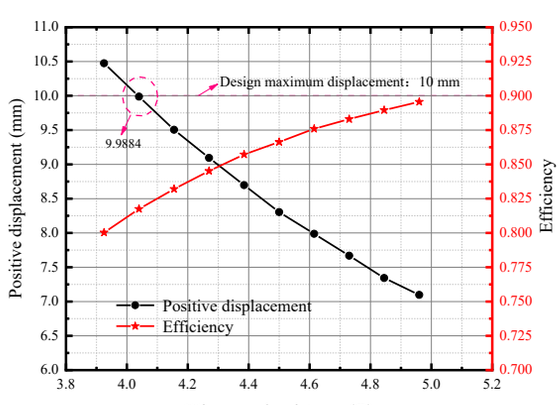

Fig. 7　Compressor lightweight selection
图 7　压缩机轻量化优选

2.3　Low temperature JT heat transfer system

The key to realizing 500 mW@4.2 K is the design of a tube-in-tube heat exchanger with high efficiency and low-pressure drop. The fluid has a certain pressure drop in the high-pressure channel of the counter current casing heat exchanger at all stages and the reflux fluid in the whole low-pressure channel to varying degrees. Therefore, in the energy equation, it is considered that the enthalpy of the fluid is not only related to temperature but also a function of pressure [31]. Select the high-pressure channel, low-pressure channel and the fluid contained therein as control bodies for calculation. Each control body is composed of high-pressure fluid (HPF), wall material between high and low-pressure fluid and low-pressure fluid (LPF).

For the low-pressure drop, we found that the pressure drop of the low-pressure channel in CFHX3 is about

200 Pa. For a helium JTC operating at 4.2 K, the pressure at its evaporator is usually about 100 kPa, and the pressure drops only accounts for about 0.2% of the low-pressure. In addition, the following calculation shows the effect of pressure drop on the theoretical cooling capacity. The theoretical cooling capacity of helium JTC can be calculated as [32]:

$$Q_c = \dot{m} \cdot q_c = \dot{m} \cdot \min[(h_{T_{pre2},P_L} - h_{T_{pre2},P_h}),(h_{P_L,Q=1} - h_{T_h,P_h})], \quad (18)$$

where $\dot{m}$ represent the mass flow rate; q_c represent the unit cooling capacity, which is determined by T_{pre2}, P_h and P_L. When T_{pre2} is 15 K, P_h is 1.6 MPa, $\dot{m}$ is 45 mg/s, the theoretical cooling capacity is 502.55 mW when the low-pressure is 100 kPa, respectively.

The analysis of energy transfer and exchange between control bodies is very important: the energy transferred by high-pressure fluid to materials is Q_{hw}; the energy obtained by the material includes: Q_{hw} and the difference of heat introduced or exported due to axial heat conduction Q_a. Then the material transfers all the absorbed energy into the low-pressure fluid, namely Q_{wl}; at the same time, because the low-pressure fluid is outside the heat exchanger, the radiation heat transfer from the cold shield to the heat exchanger is added to the low-pressure fluid. The radial thermal resistance of the material is ignored, so the temperature of the same section can be assumed to be approximately uniform. At present, the casing heat exchanger with a given structure size is divided into micro-elements along the axial direction, and the step size ΔL is 1 mm.

For a microelement, the momentum and energy equations of high-pressure fluid, low-pressure fluid and wall material are established respectively. The control equations are shown in equations (19) - (23):

Momentum equation: the momentum equations are shown in equations (19) and (20). In the micro-channel structure, the calculation of pressure drop should consider not only the viscous friction loss between the fluid and the contact surface but also the pressure change caused by the change in the kinetic energy of the fluid [33-34].

$$\Delta P_h = P_{h,in} - P_{h,out} = f_h \rho_h u_h^2 \frac{\Delta L}{2de_h}, \quad (19)$$

$$\Delta P_l = P_{l,in} - P_{l,out} = -f_l \rho_l u_l^2 \frac{\Delta L}{2de_l}. \quad (20)$$

Energy equation: the difference of the sum of enthalpy and kinetic energy between the fluid at the inlet and outlet is the energy absorbed or released by the fluid. The enthalpy is a function of temperature and pressure.

$$Q_{h-w} + Q_a = Q_{w-l}, \quad (21)$$

$$H_{h,in} + E_{h,in} = H_{h,out} + E_{h,out} + Q_{h-w}, \quad (22)$$

$$H_{l,in} + E_{l,in} + Q_{w-l} + Q_r = H_{l,out} + E_{l,out}. \quad (23)$$

The calculation equations of pressure drop, heat transfer and of two-phase flow are shown in Table 3:

Figure 8 shows the convective heat transfer between the fluid and the wall. It can be seen that the heat exchange Q along the way increases first, reaches the peak value and then decreases gradually. From the perspective of high-pressure fluid, the convective heat transfer coefficient and the heat transfer temperature difference increased in the front section, so the heat transfer gradually increased, and the rising trend became faster until it reached the peak of 1.15 mW at 625 mm. Subsequently, due to the rapid decrease of heat exchange temperature difference and convective heat transfer coefficient, the heat exchange also decreased rapidly. Therefore, the length design parameters of the maximum heat transfer coefficient are obtained to complete the efficient heat exchange optimization design of the casing heat exchanger.

2.4 Comparison of previous experiments in 0.1 W@4 K

The design specifications state that the cooling capacity must be greater than 0.3 W@4.2 K (23 ± 5 °C),

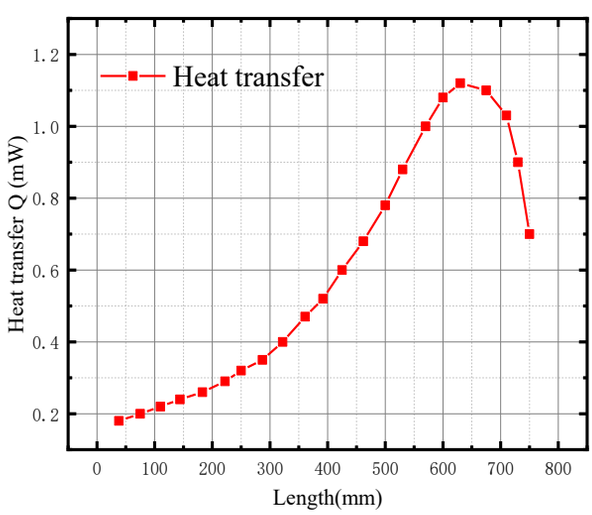

Fig. 8 Effect of length on heat transfer efficiency
图 8 长度对换热效率的影响

Table 3 Selected correlation expression and applicable scope
表 3 相关计算式与其应用范围

Calculation range	Correlation	Applicable type
$0<Re<3000$	$f = 0.076Re^{-0.25} + 0.00725(\frac{d}{D})^{0.5}$	Laminar flow
$Re>3000$	$f = (1.82\lg Re - 1.64)^{-2}$	Circular tube
$150<Re<120000, 0.5<Pr<2000$	$Nu = 3.66 + 0.014Re^{0.86}\mathrm{Pr}^{0.4}$	Coil
Re>10000	$h = 0.023C_pGRe^{-0.2}Pr^{-\frac{2}{3}}$ $f = 0.184Re^{-0.2}$	Homogeneous model of two-phase flow

have an input power of less than 1.8 kW, and weigh less than 27 kg. Given the redundancy, the cooling capacity ought to be 0.5 W@4.2 K, and the input power ought to be less than 1.6 kW. The design of the system structure is depicted in Fig. 9.

We developed an experiment bench of the 0.1 W@4.1 K previous prototype of the cryocooler system, and its external structures are shown in Fig. 10, respectively. The first-stage SC and second-stage STPC can provide 15 W@80 K and 0.9 W@15 K cooling performance which meets the precooling requirements of helium JTC. The JT compressor unit is composed of multiple linear direct current compressors, each of which can achieve a pressure ratio of about 3 to 5. By connecting each JT compressor in series, a higher-pressure ratio can be achieved to meet the high-pressure and pressure required by the JT cycle [35].

Experiments on the previous 0.1 W@4.1 K prototype of the cryocooler system have validated the system's design method, as shown in Table 4.

Once the cooling performance target of 0.5 W @ 4.2 K, a secondary pre-cooling temperature of 15 K and a high-pressure of 1.6 MPa have been determined. The required mass flow rate can be calculated, and the formula is as follows:

$$\dot{m} = \frac{Q_c}{q_c}, \tag{24}$$

where $\dot{m}$ (mg/s) represent the mass flow rate, Q_c (W) represent the unit cooling capacity, and q_c (J/kg) represent the unit cooling capacity. The trends in second-stage pre-cooling temperature, high-pressure, and mass flow rate for the 0.5 W @ 4.2 K design target are given in Fig. 11. It can be seen that the required mass flow rate increases as the second-stage pre-cooling temperature increases when the high-pressure is certain. Due to

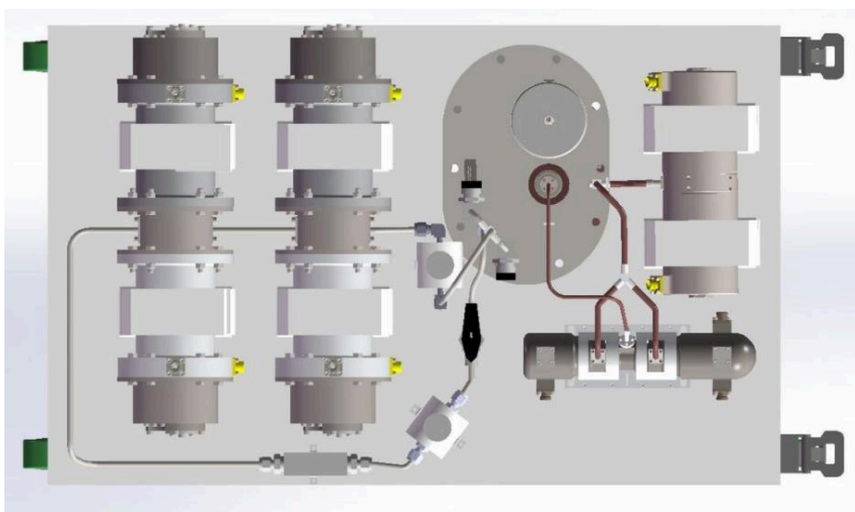

Fig. 9　0.3 W@4.2 K JT cryocooler system structures design
图 9　0.3 W@4.2 K节流制冷系统的结构设计图

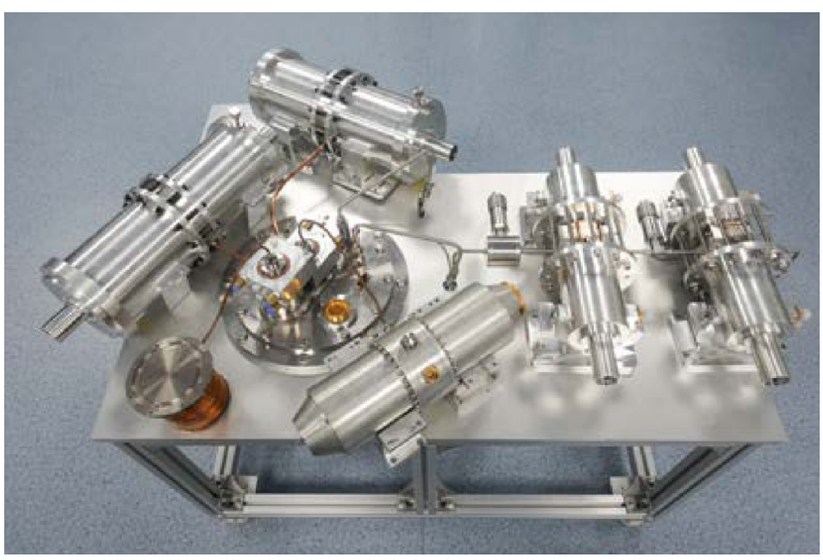

Fig. 10　0.1 W@4.1 K JT cryocooler system experimental setup
图 10　0.1 W@4.1 K节流制冷系统实验台

Table 4 Comparison of system performance parameters
表 4 系统性能参数对比

	0. 1 W@4. 1 K Design value	0. 1 W@4. 1 K Measure results	0. 3 W@4. 2 K Design value
Input power	700 W	647 W	1800 W
Cooling capacity	150 mW@4. 1 K	110 mW@4. 1 K	500 mW@4. 2 K
Mass flow	17 mg/s	14. 1 mg/s	45 mg/s
First-stage temperature	83. 9 K	83. 1 K	80 K
Second-stage temperature	20. 0 K	17. 5 K	15 K

the optimum high-pressure, the mass flow rate tends to decrease and then increase for a given second-stage pre-cooling temperature, and there exists a minimum mass flow rate. From the results of the calculation and analysis, the helium JTC was selected to have a minimum mass flow rate of 45 mg/s at a pre-cooling temperature of 15 K and a high-pressure of 1. 6 MPa, which can achieve a cooling capacity of 0. 5 W.

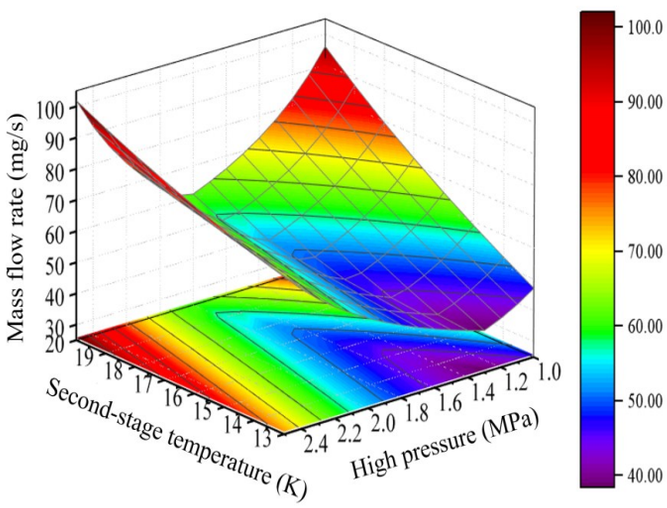

Fig. 11 Relationship between second-stage temperature, high-pressure and mass flow rate at 0. 5 W @ 4. 2 K
图 11 0. 5 W @ 4. 2 K时,第二级预冷温度、高压压力和质量流量之间的关系

When tripling the mass flow and input power of the JT system, and decreasing the pre-cooling temperature, the JTC system can reach 0. 3 W at 4. 2 K. Based on a new design concept, it will have three times the cooling capacity, indicating that it will have a substantial cooling capacity.

3·Interconnection with BIB detector

The fluctuating temperature of the helium JTC has a correlation with the change in ambient temperature, but the change in ambient temperature will also affect the performance of the cryocooler, resulting in the change of pre-cooling temperature at all levels. Consequently, the temperature fluctuations of the helium JTC are caused by environmental temperature fluctuations and are also influenced by the temperature fluctuations of the two-stage pre-cooling temperatures.

Epitaxial growth and ion implantation are two typical techniques to develop the BIB device. The epitaxial detector could be understood as the vertical detector. According to where the infrared signal illuminates, the vertical detector is divided into two architectures: back-illuminated (BSI) and topside-illuminated (TSI) architecture, as shown in Figure 12(a) and 12(b), respectively. The BSI BIB architecture is usually epitaxially grown on an intrinsic Si substrate by chemical vapor deposition (CVD). The epitaxial structure comprises a bottom contact layer, a reasonably doped active (absorbing) layer (AL), and a high-purity blocking layer (BL). Figure 12 (b) shows the TSI device structure. The doped AL is sandwiched between a Si substrate and an ultrapure BL. Ion implantation is also developed to construct the AL and contact layer to form the BIB detector. However, the AL of the ion-implanted device is relatively shallow limited by the implant energy, which could be named the planar architecture as shown in Fig. 12(c).

Figure 12 (d) illustrates the schematic structures and band diagrams of n-type BIB detectors. The doped AL and the pure BL are between the degenerate contact layers. At the same time, there is a low concentration of non-intentionally p-doping (NA) in AL. To form the impurity band, the general magnitude of the n-type dopant of AL is approximately 1017 cm^{-3}. Figure 12 (d) also shows that the electrons of the impurity band could be swept to the AL contact when the BL contact is positively biased. Meanwhile, the positive donors (D+) will move in another direction (hopping conduction). The BL could stop the injection of new D+ because of the discontinuity of the impurity band, which suppresses the dark current.

When the temperature rises, the electrons originally bound around the impurity atoms are thermally ionized to the conduction band, which contributes a large thermal noise as shown in Fig. 12(d). At the same time, the temperature-sensitive mechanism of BIB detectors has revealed that the photoresponse of the BIB detector dramatically reduces under rising temperature [36]. The negative charge concentration that varies significantly with temperature in the depletion region increases, leading to a more narrowly depletion. For BIB devices, only the photo-carriers generated from the depletion would successfully transport to the contact and contribute photocurrent and photoresponse. The electrical field and depletion region width are calculated as shown in Figure12(e) and 12 (f). The latter rapidly decreases under higher temperatures, resulting in a significant reduction in the detector extrinsic-photoresponse.

The result of the 0. 1 W@4. 1 K experiment indi-

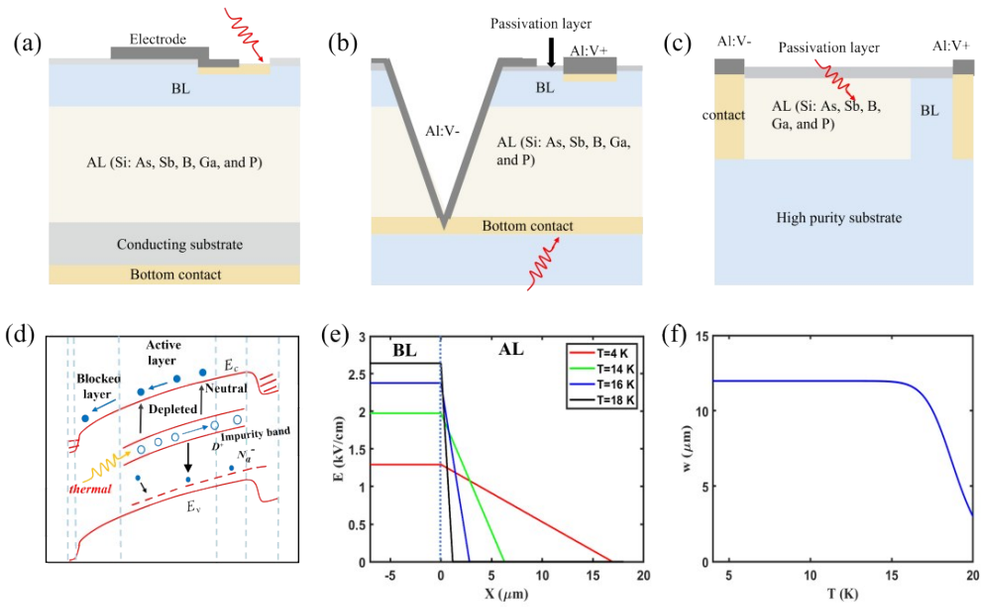

Fig. 12　(a) Structure of topside-illuminated (TSI) vertical BIB detectors, (b) structure of back-illuminated (BSI) vertical BIB detectors, (c) structure of ion-implanted BIB detectors, (d) detector band diagram under positive bias with thermal incidence, (e) electric field intensity as a function of position at different temperatures, (f) the relationship between the depletion region width with temperature.

图 12　(a) 正入射垂直BIB探测器结构, (b) 背入射BIB探测器结构, (c) 离子注入型BIB探测器结构, (d) 红外光照时正偏压下的器件能带示意图, (e) 不同温度下电场强度与位置的关系 (f) 耗尽区宽度与温度的关系

cates that the temperature of the evaporator that provides cooling capacity for the BIB detector fluctuates by 6 mK in Fig. 13. Using the PID active temperature control technology with the parameters KP=15, KI=0.01, and KD = 0.1, we were able to reduce the temperature fluctuation range to 2 mK, resulting in a more stable cold head temperature for the BIB detector.

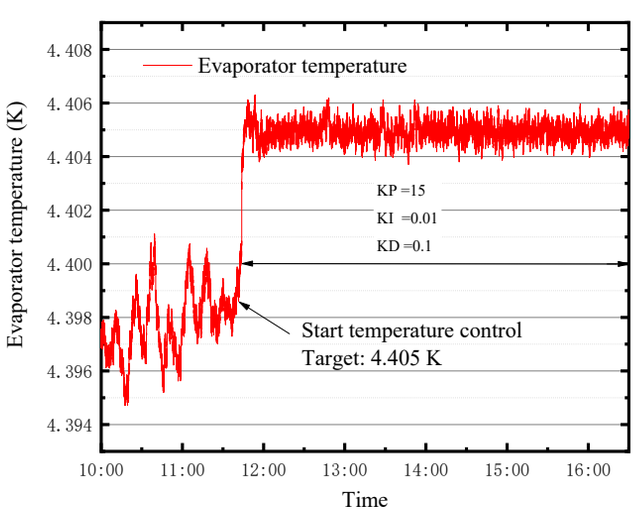

Fig. 13　Temperature fluctuations and control

图 13　温度波动及其控制

4　Conclusion

By comparing with the previous experimental system of 0.1 W@4.1 K, an optimized cryogenic system is introduced for obtaining a large cooling capacity at 4.2 K with high efficiency. The efficiency and lightweight design are completed within 30 kg, and the input power is within 1.8 kW. We optimize and enhance each component of the cryocooler system:

(1) The performance of the two-stage pre-cooling system is consistent and its cooling capacity is substantial. It comprises a Stirling cryocooler for 80 K and a Stirling-type pulse tube cryocooler for 15 K. Adjusting the frequency achieves the maximum COP and cooling capacity of the second-stage pulse tube. By simulating the rigidity and rod diameter of the SC, the optimal combination can be determined.

(2) A double-piston opposed VLC is used in the JT cycle, to generate a pressure of 0.1 MPa. By reducing the radial thickness of the inner pole, the outer diameter of the magnetic circuit is decreased, bringing the motor current close to its critical value, thereby minimizing the motor's volume and weight. The VLC can get a total pressure ratio of 18.9 and a mass flow rate of 53 mg/s.

(3) For the JT cycle, the specific heat transfer process was analyzed. Then, we determined the optimal relationship between the length and the heat transfer coefficient, which will improve the performance of the heat transfer solution. Using the results of previous experiments, enhance the system's design to achieve a high cooling capacity of 0.3 W at 4.2 K and a lightweight design.

Through the integration design of the JT system, the cooling performance of 0.3 W@4.2 K with an input power of 1.8 kW can be obtained. To further improve the cooling performance, the optimal parameters to obtain

the maximum cooling capacity under minimum input power need to be investigated in detail. The study can provide cryogenic technology guarantees for the coming space large array BIB detectors.

Reference

[1] Deng K, Zhang K, Li Q, *et al*. High-operating temperature far-infrared Si: Ga blocked-impurity-band detectors [J]. *Applied physics letters*, 2022(21):120.

[2] GUO Jia-Xiang, XIE Run-Zhang, WANG Peng, *et al*. Infrared photodetectors for multidimensional optical information acquisition [J]. *J. Infrared Millim and Waves*, 2022, **41**(1):40~60.

[3] Y. Xiao, H. Zhu, K. Deng, *et al*. Progress and challenges in blocked impurity band infrared detectors for space-based astronomy, Sci. China-Phys. *Mech. Astron*. 65, **287301** (2022)

[4] SHI Qian, ZHANG Shu-Kui, WANG Jian-Lu, *et al*. Progress on nBn infrared detectors [J]. *J. Infrared Millim. Waves*, 2022, **41**(1): 139~150.

[5] Weida, Hu, Zhenhua, *et al*. 128×128 long-wavelength/mid-wavelength two-color HgCdTe infrared focal plane array detector with ultralow spectral cross talk [J]. *Optics Letters*, 2014, **39**(17). DOI: 10.1364/ol.39.005184.

[6] Hu W D, Chen X S, Ye Z H, *et al*. A hybrid surface passivation on HgCdTe long wave infrared detector with in-situ CdTe deposition and high-density hydrogen plasma modification [J]. *Applied Physics Letters*, 2011, **99**(9):091101-091101-3. DOI: 10.1063/1.3633103.

[7] Z.-H. Gan, B. Wang, D.-L. Liu, *et al*. Status and development trends of space mechanical refrigeration system at liquid helium temperature, Journal of Zhejiang University. Engineering Science, 46 (12) (2012) 2160-2177.

[8] GAN Zhi-hua, TAO Xuan, LIU Dong-li, *et al*. Development status of space cryogenic technology atliquid helium temperature in Japan. Journal of Zhejiang University. *Engineering Science*, 49(10) (2015) 1821-1835.

[9] D. Liu, Z. Gan, A. de Waele, *et al*. Temperature and mass-flow behavior of a He-4 Joule-Thomson cryocooler, International Journal of Heat and Mass Transfer, 109 (2017) 1094-1099.

[10] Salomonovich A E, Sidyakina T M, Khaikin A S, *et al*. Space helium cryocooler [J]. *Cryogenics*, 1981, **21**(8):474-478.

[11] Inatani J, Narasaki K, Tsunematsu S, *et al*. Mechanical cryocooler and cryostat for submillimeter SIS mixer receiver in space [J]. *Proc Spie*, 2001, **4540**:197-208.

[12] Ross, Jr, R, *et al*. NASA's Advanced Cryocooler Technology Development Program (ACTDP). [J]. *AIP Conference Proceedings*, 2006, **823**(1):607-614.

[13] Glaister D S, Gully W, Ross R, *et al*. Ball Aerospace 4-6 K Space Cryocooler [J]. *Aip Conference Proceedings*, 2006.

[14] Banks Kimberly, Larson Melora, Aymergen Cagatay, *et al*. James Webb Space Telescope Mid-Infrared Instrument cryocooler systems engineering [J]. *NASA Goddard Space Flight Ctr.* (*United States*); Jet Propulsion Lab. (United States); SGT, Inc. (United States), 2008,7017.

[15] Petach M, Durand D, Michaelian M, *et al*. MIRI cryocooler system design update [C]. Miller S D, Ross Jr R G. Cryocoolers. Boulder, CO: Springer Science & Business Media, Inc., 2011:9-12.

[16] Quan J, Zhou Z J, Liu Y J, *et al*. A miniature liquid helium temperature JT cryocooler for space application [J]. *Science China Technological Sciences*, 2014, **57**(11): 2236-2240.

[17] Zhenjun Zhou. Research on 4K throttling cryocooler with high frequency multistage pulse tube pre-cooling [D]. Technical Institute of Physics and Chemistry, 2014.

[18] Sato Yoichi, Tanaka Kosuke, Sugita Hiroyuki, *et al*. Lifetime test of the 4K Joule-Thomson cryocooler [J]. *Cryogenics*, 2021(prepublish).

[19] Liao K S, Li N, Wang C, *et al*. Extended mode in blocked impurity band detectors for terahertz radiation detection [J]. *Applied Physics Letters*, 2014, **105**(14):183903-65.

[20] Wang, Y L, Liu, D L, Gan, Z H, *et al*. Cooling-capacity characteristics of Helium-4 JT cryocoolers, IOP Conference Series. Materials Science and Engineering; Ol.278, Iss.1, (Dec 2017).

[21] Hejun Hui, Jiantang Song, Shaoshuai Liu, *et al*. Energy conversion efficiency improvement of a Stirling type PTR for dual temperature cooling by adopting two active work-recovery phase shifters, International Journal of Refrigeration, 2022, *ISSN 0140*-7007.

[22] Zhi X, Qiu L, Pfotenhauer J M, *et al*. cryogenic mechanism of the gas parcels in pulse tube cryocoolers under different phase angles [J]. *International Journal of Heat & Mass Transfer*, 2016, 103 (dec.): 382-389.

[23] Zhi X. Q, *Han, L.*, Dietrich, M., *et al*. A three-stage Stirling pulse tube cryocooler reached 4.26 K with He-4 working fluid, cryogenics, 2013-12, 58, 93-96.

[24] Wei D, Luo E, Wang X, *et al*. Impedance match for Stirling type cryocoolers [J]. *Cryogenics*, 2011, **51**(4):168-172.

[25] Wei Dai, Guoyao Yu, Shanglong Zhu, *et al*. A 300 Hz thermoacoustically-driven pulse tube cryocooler for temperature below 100 K, Applied Physics Letters, Vol.**90**, 024104, 2007.

[26] YIN Wang, WU Wenting, HUI Hejun, *et al*. Theoretical and Experimental Study on the Length-Diameter of the Regenerator in the Low Temperature Section of a 15 K Thermal-Coupled Two-Stage Pulse Tube Cryocooler [J]. *Journal of Xi'an Jiaotong University*, 2022, **56** (12):184-194.

[27] Wang X, Jian Z, Shuai C, *et al*. Study on a high capacity two-stage free piston Stirling cryocooler working around 30 K [J]. *Cryogenics*, 2016, **80**:193-198.

[28] Wang Bo, Chao Yijun, Wang Haoren, *et al*. A miniature Stirling cryocooler operating above 100Hz down to liquid nitrogen temperature, Applied Thermal Engineering, Volume 186, 2021, 116524, ISSN 1359-4311.

[29] Guo Y, Chao Y, Wang B, *et al*. A general model of Stirling cryocoolers and its verification [J]. *Energy Conversion and Management*, 2019, 188(MAY):54-65.

[30] Zhi X. Study on the output pressure amplitudes of the linear compressor based on the complex vector analysis method [J]. *International Journal of Refrigeration*, 2019, 107.

[31] Y.L. Wang, D.L. Liu, Z.H. Gan, *et al*. Cooling-capacity characteristics of Helium-4 JT cryocoolers, (2017).

[32] Y. Shen, D. Liu, S. Chen, *et al*. Study on cooling capacity characteristics of an open-cycle Joule-Thomson cryocooler working at liquid helium temperature, Applied Thermal Engineering, 166 (2020) 114667.

[33] Z. Chen, S. Liu, Y. Wu, *et al*. Performance testing and temperature fluctuations of a 4.5 K@ 150 mW Joule-Thomson closed cycle cryocooler for space applications, in: IOP Conference Series: Materials Science and Engineering, IOP Publishing, **2022**, pp. 012017.

[34] Z. Chen, X. Cui, S. Liu, *et al*. Study on cooling capacity characteristics of a helium Joule-Thomson cryocooler, Applied Thermal Engineering, 221 (2023) 119820.

[35] Zhichao Chen, Shaoshuai Liu, Zhenhua Jiang, *et al*. Helium Joule-Thomson cryocooler below 4.5 K for infrared detectors, Proc. SPIE 12505, Earth and Space: From Infrared to Terahertz (ESIT 2022), **125051**Y (31 January 2023); doi: 10.1117/12.2665290

[36] Zhu H, Zhu J, Hu W, *et al*. Temperature-sensitive mechanism for silicon blocked-impurity-band photodetectors [J]. *Applied physics letters*, 2021(19):119.